Journal of Marine Science and Technology

Volume 31 | Issue 4 Article 13

Numerical analysis of impact vibration based on a bifurcation diagram with two varying control parameters

June-Yule Lee
Department of Marine Engineering, National Kaohsiung University of Science and Technology 482, Jhong-Jhou 3rd Road, Cijin District, Kaohsiung City 805301, Taiwan, juneyule@nkust.edu.tw

Recommended Citation

Lee, June-Yule (2023) "Numerical analysis of impact vibration based on a bifurcation diagram with two varying control parameters," *Journal of Marine Science and Technology*: Vol. 31: Iss. 4, Article 13.
DOI: 10.51400/2709-6998.2720
Available at: https://jmstt.ntou.edu.tw/journal/vol31/iss4/13

RESEARCH ARTICLE

Numerical Analysis of Impact Vibration Based on a Bifurcation Diagram With Two Varying Control Parameters

June-Yule Lee

Department of Marine Engineering, National Kaohsiung University of Science and Technology, Kaohsiung City, Taiwan

Abstract

This study investigates impact vibration by using a bifurcation diagram with one or two varying control parameters. Sticking, periodic, and chaotic motions are explored using the Poincaré mapping and impact mapping techniques. A full range of bifurcation diagrams with varying driving frequencies is obtained, and the statistical index of the standard deviation (*Std*) is used to calculate the impact series in the bifurcation diagrams. The results indicate strong agreement between impact conditions and their corresponding statistical index values for the *Std*. Subsequently, the *Std* values for two control parameters of (*w*, *m*), (*w*, *c*), (*w*, *k*), (*w*, *f*), and (*w*, *r*) are obtained. The generated three-dimensional plots display a mountain-like area indicating unstable regions and a flat area indicating stable regions. The corresponding contour plots display the boundary of the stable and unstable regions in two-parameter domains. These findings expand our understanding of impact vibration and how it benefits condition monitoring.

Keywords: Impact vibration, Impact map, Poincaré map, Bifurcation diagram

1. Introduction

Impact vibration generally occurs in systems with clearances. In marine engineering, the presence of clearances or motion constraints enable the expansion or contraction of various mechanical components. In the long term, impact vibration adversely affects system performance by increasing noise level, intensifying fatigue, and causing wear and break. Goyder and The [1] studied the impact vibration of heat exchanger tubes at their supported points, Jian and Zhang [2] modelled a bearing vibration system used to monitor health conditions, Kadmiri et al. [3] analysed the rattling noise caused by an automotive gearbox, Moosavian et al. [4] detected piston scuffing fault by conducting impact vibration analysis, and Cheng et al. [5] analysed the nonlinear dynamics involved in the application of a rotor-bearing-coupling system.

Impact dynamics is highly relevant to ship docking and offshore structures. Thompson [6] studied the motion of a ship against a seawall and analysed the complex dynamics underlying this motion. Grace et al. [7,8] analysed the impact dynamics of ships with one-sided barriers; that study developed a model for simulating the rolling motion of a ship interacting with ice, and experimental validation was performed in a towing tank with a flap-type wave generator. Chen et al. [9,10] have investigated the installation of a float-over desk based on a heave-roll-pitch impact model and how the end-stop mechanism affects a point absorber in regular waves. Finally, Guo and Ringwood [11] modelled a wave energy converter based on linear buoy interaction and a nonlinear impact mechanism.

In the past, impact system models have been regarded as soft or hard impact models. In a soft impact model, the impact base is modelled using a spring-damper support; in such a case, the time of

Received 7 May 2023; revised 4 November 2023; accepted 10 November 2023.
Available online 15 December 2023
E-mail address: juneyule@nkust.edu.tw.

https://doi.org/10.51400/2709-6998.2720

impact is nonzero, and the colliding body can penetrate the impact base. In a hard impact model, the impact base and colliding body are stiff; an impact is treated as instantaneous, and its restitution coefficient is used to represent energy dissipation. Hunt and Crossley [12] asserted that contact force models are a key factor in the modelling and analysis of impact systems. The kinematic coefficient of restitution is determined by obtaining the ratio of the impacting velocity just after an impact to that just before an impact. For a complete elastic impact, this parameter is equal to one, whereas for a complete inelastic impact, the restitution coefficient is zero. Silva et al. [13] provided a detailed review of the literature regarding contact force models.

In recent years, several studies of fundamental impacting motions based on the impact rule of the restitution coefficient have focused on theoretical dynamics, particularly in the context of chaotic phenomena. Shaw and Holmes [14] assessed a periodic forced piecewise linear oscillator and demonstrated its ability to observe saddle node and flip bifurcations. Nordmark [15,16], Foale and Bishop [17], and Chillingworth [18] have studied low-velocity collisions and the grazing effect and have revealed the presence of bifurcation. Budd and Dux [19,20] and Lee [21] have examined chattering vibration with sticking motions. Samukham et al. [22] modelled the non-smooth impact motion of a continuous structure against a rigid distributed obstacle. Finally, Skurativskyi et al. [23] and Witkowski et al. [24] have employed an experimental model to investigate a forced impacting oscillator. In the aforementioned studies, chaotic impact series have been studied statistically, and impacting features have been identified in both numerical and experimental results.

For some engineering applications, chaotic impact vibrations are harmful and cause system damage. Chaotic motion is caused by changes in multiple parameters of an impact system. To address this problem, Lee and Yan [25] demonstrated that unstable chaotic impact oscillators can be controlled and maintained in a desired position through a synchronization scheme. Chang et al. [26] proposed a state feedback control technique for a chaotic magnetic levitation system. Wei et al. [27] studied the chaos control system of an impact oscillator by applying a data-driven method, and they verified the effectiveness and feasibility of the system through simulation results.

The present study examines the motion behaviours of an impact oscillator with a two-parameter-control scheme; this scheme is an extension of the one-parameter-control scheme proposed by Lee [21]. In addition, a complete range of relevant bifurcation diagrams is plotted through Poincaré and impact mapping. Subsequently, the statistical index of the standard deviation (*Std*) in the

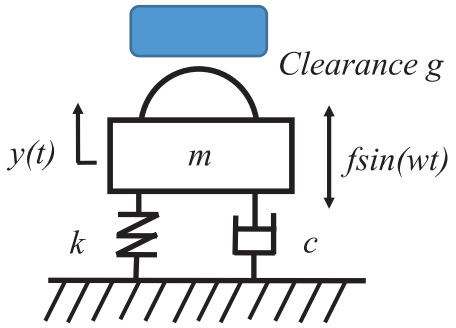

Fig. 1. Impact vibration with a one-side constraint.

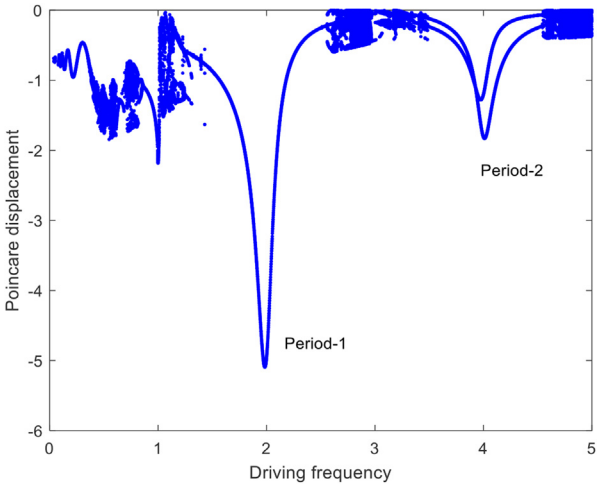

Fig. 2. Bifurcation diagram of change in Poincaré displacement with varying driving frequency.

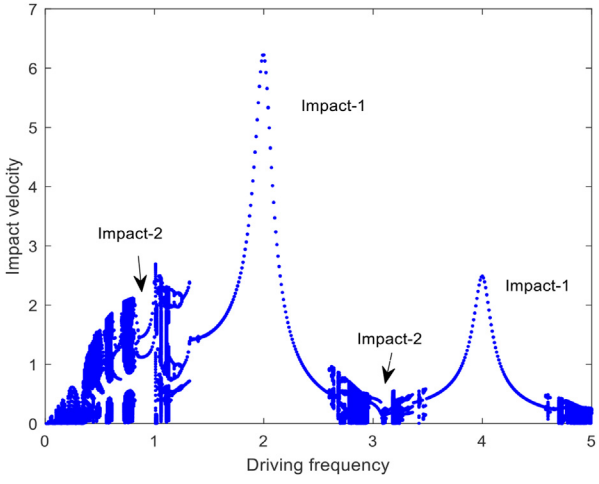

Fig. 3. Bifurcation diagram of change in impact velocity with varying driving frequency.

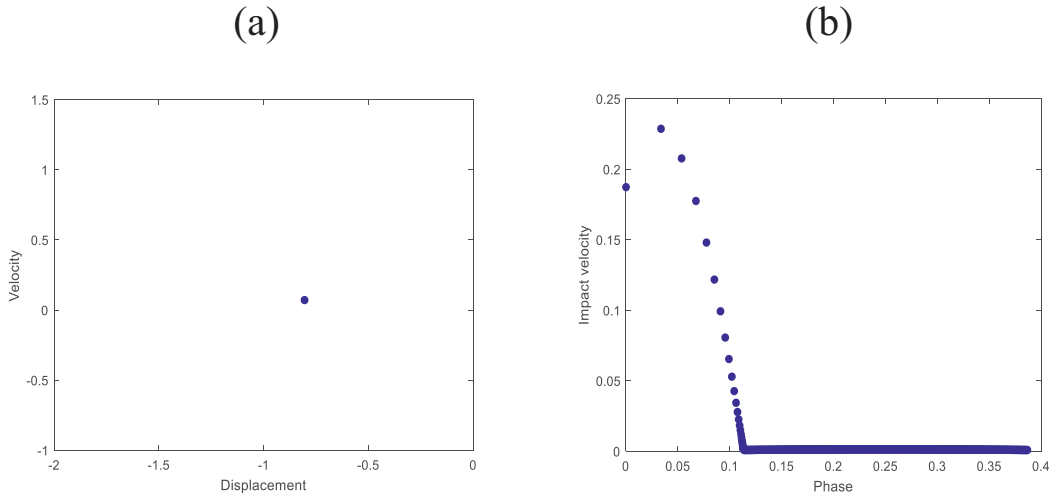

Fig. 4. Impact vibration when driving frequency w = 0.10: (a) Poincaré map; (b) impact map.

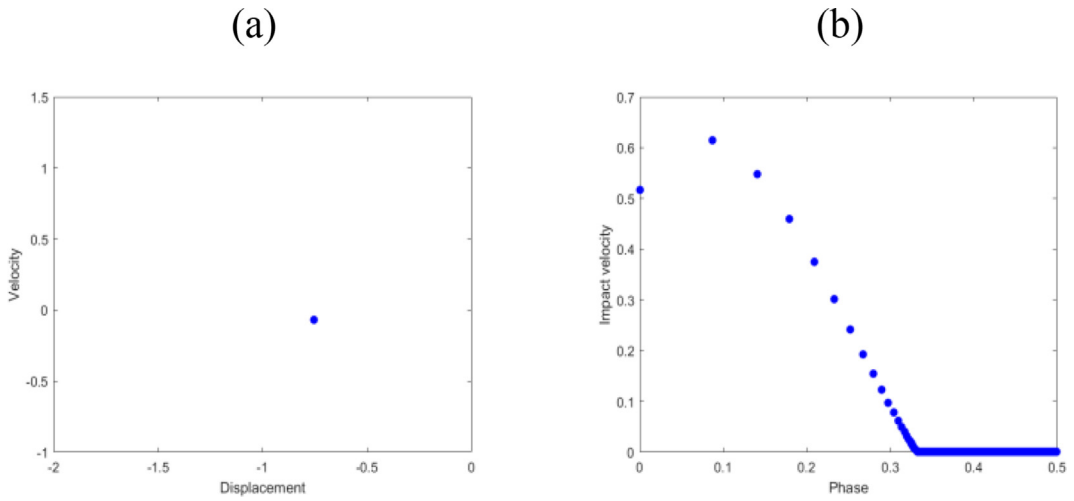

Fig. 5. Impact vibration when driving frequency w = 0.25: (a) Poincaré map; (b) impact map.

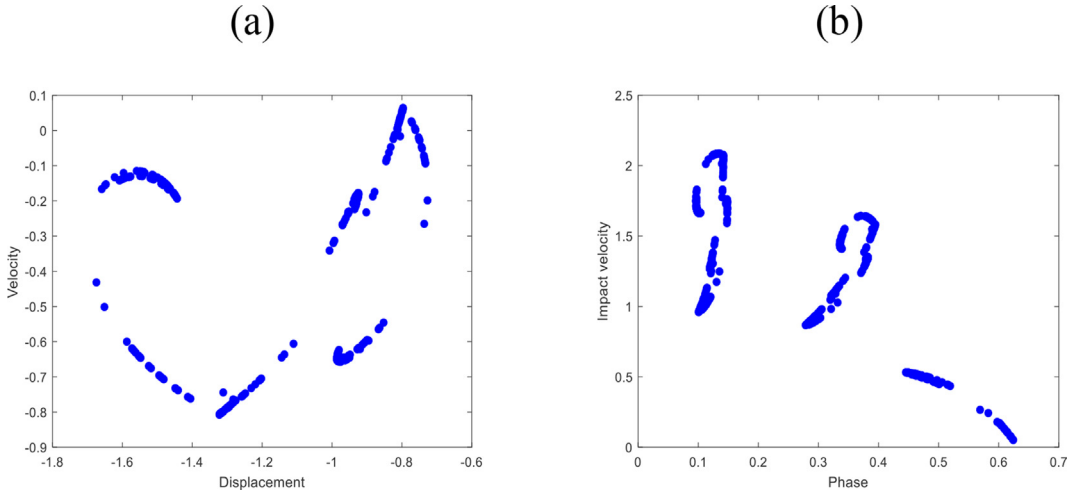

Fig. 6. Impact vibration when driving frequency w = 0.75: (a) Poincaré map; (b) impact map.

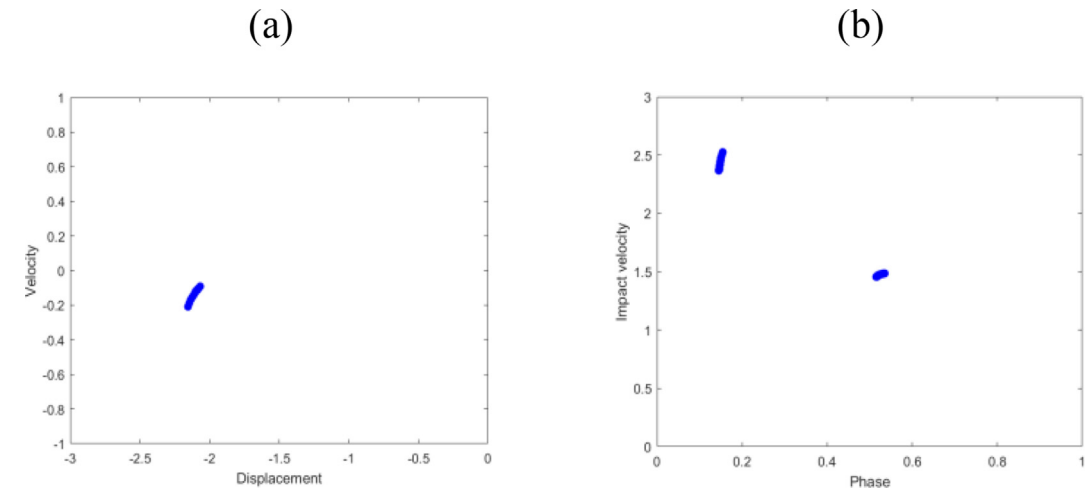

Fig. 7. Impact vibration when driving frequency $w = 1.0$: (a) Poincaré map; (b) impact map.

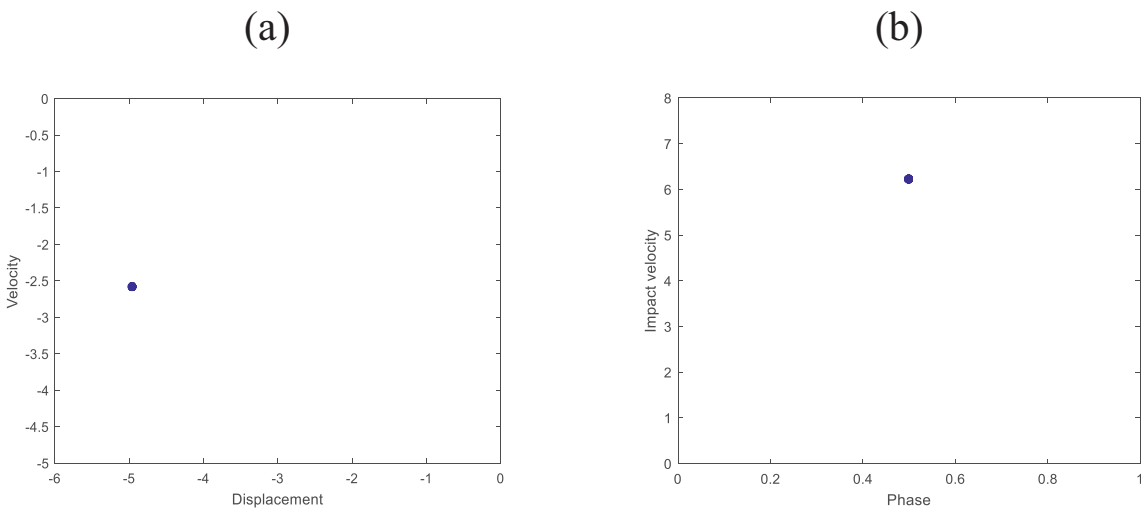

Fig. 8. Impact vibration when driving frequency $w = 2.0$: (a) Poincaré map; (b) impact map.

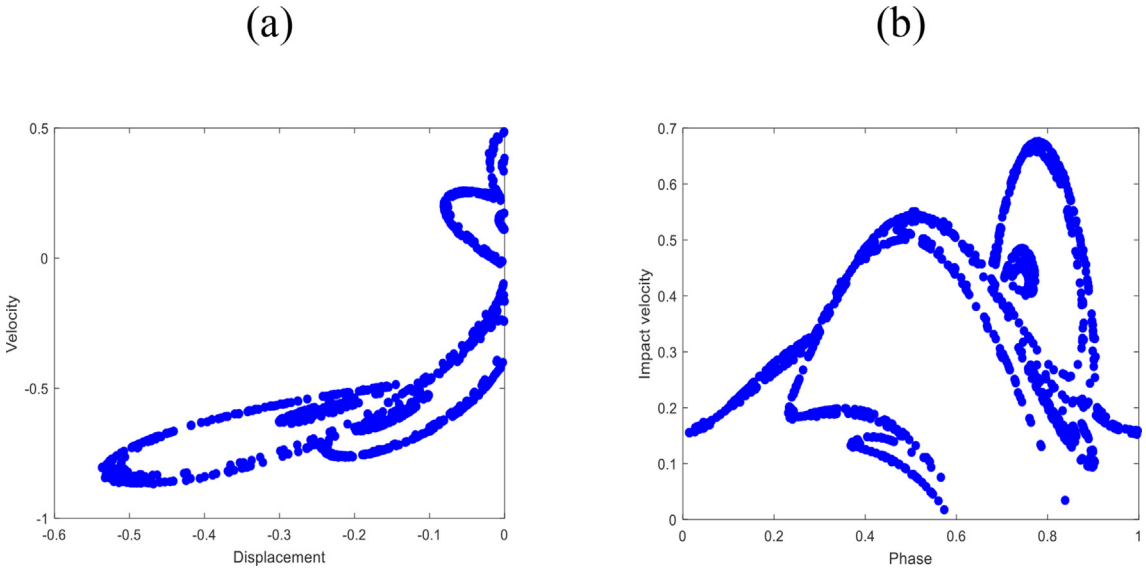

Fig. 9. Impact vibration when driving frequency $w = 2.8$: (a) Poincaré map; (b) impact map.

generated map is calculated and used as an indicator for a two-parameter control domain. In particular, the influences on impact vibration are evaluated by controlling the driving frequency and five other parameters, namely mass, damping, stiffness, forcing amplitude, and the restitution coefficient.

The remainder of the present paper is organized as follows: Section 2 describes the mathematical modelling of impact vibration and the analysis techniques employed in this study. Section 3 presents one control parameter of a bifurcation diagram. Specifically, the numerical solutions for impact vibration—including sticking motion, periodic motion, chaotic motion, and impact resonance—are characterised using Poincaré mapping, impact mapping, and several statistical techniques. Section 4 presents the two-parameter control of the statistical index on an impact map, and the contour plots of the stable and unstable boundaries are identified within a two-parameter space. Finally, Section 5 provides conclusions to the present study.

2. Mathematical modelling and analysis techniques

An illustration of an impact vibration model with a one-side constraint is presented in Fig. 1. In this model, the oscillator is excited by a sine wave, and the motion is constrained by clearance. This impact is treated as instantaneous, and the equation of motion when no impact is present is expressed as follows:

$$m\ddot{y} + c\dot{y} + ky = f\sin(wt), \mathrm{y} < g \tag{1}$$

where $\ddot{y}$ is the acceleration, $\dot{y}$ is the velocity, y is the displacement, m is the mass, c is the damping, k is the stiffness, f is the forcing amplitude, w is the driving frequency, and g is the clearance. The impact occurs at $y(t) = g$, and the corresponding impact velocity is simulated as $\dot{y}(t^+) = -r\dot{y}(t^-)$, where r is the restitution coefficient, (t^-) is the time immediately before impact, and (t^+) is the time immediately after impact.

In the investigation described in this paper, the numerical integration of the fourth order Runge-Kutta algorithm is applied to Eq. (1), and the time

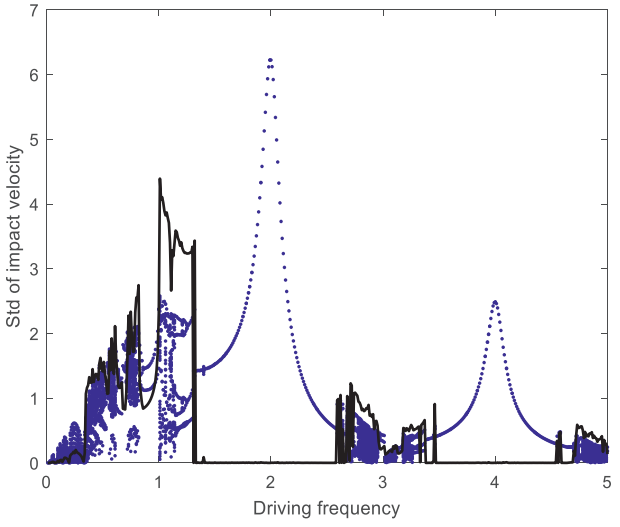

Fig. 10. Bifurcation diagram (blue dots) and Std values (black lines) of impact velocity in impact map with varying driving frequency.

(a)

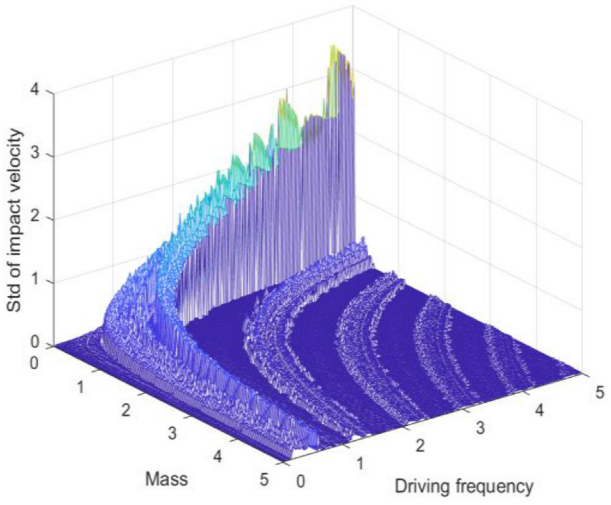

(b)

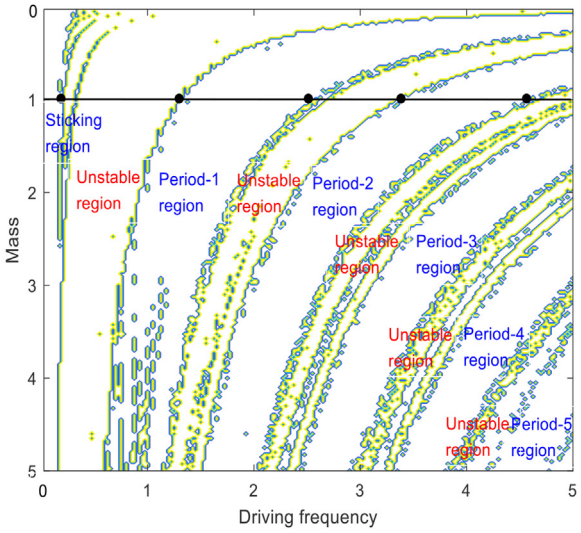

Fig. 11. Stable and unstable boundaries in (w, m) domain.

step is set as 0.0005 s. In addition, Poincaré mapping and impact mapping are applied to verify the stability of the obtained solutions. The Poincaré map is a point set at a fixed section, namely $(y(t)_{\varphi}, \dot{y}(t)_{\varphi})$, where $\varphi = t$ modulo T and where $T = 2\pi/w$. Thus, a periodic motion displays a single point set in return maps, and a sub-periodic motion of order n has a set of n points set in the same return maps. Under chaotic conditions, a fractal point set appears in the Poincaré map.

When an impact occurs at time t_{impact} and when the displacement $y(t_{impact}) = g$, the impact map records a point set at section $(\dot{y}(t_{impact}), \Psi_{impact})$, where $\dot{y}(t_{impact})$ represents the impact velocity and where $\Psi_{impact} = t_{impact}$ modulo T. Thus, a periodic impact motion is represented by a single point set in the impact map. A sub-periodic motion of order p has a set of p points set in the impact map. Under chaotic conditions, a fractal point set appears in the impact map.

With the gradual increase or decrease of the control parameter, the bifurcation diagram reflects how a point set varies in the Poincaré map or impact map. Thus, a complete bifurcation diagram can help to predicate the stable or unstable regions for one or two control parameters.

3. Control of one parameter

In the investigation described in this paper, the parameters are set as follows: $m = 1$, $c = 0.01$, $k = 1$, $f = 1$, $r = 0.8$, and $g = 0$. In addition, the resonance of free oscillation is $w_n = \sqrt{k/m} = 1$. Simulation data are obtained between 100 and 150 s, and the data from the first 100 s are excluded to ensure a steady system state. Using the point set in the Poincaré or impact map, a full range of bifurcation diagrams can be obtained by varying the control parameter.

Fig. 2 depicts the bifurcation diagram created using the displacement in the Poincaré map. Period-n motions are characterised by the Poincaré map as variable driving frequency w values ranging from 0 to 5. The period-*1* motion and period-2 motion clearly appear at $w = 2$ and $w = 4$, respectively. Fig. 3 depicts the bifurcation diagram of the impact velocity in the impact map. The periodic impact-p motions are characterised by the impact map, where p represents the number of impacts. Fig. 3 reveals that the first and second impact resonance impact-*1* motions occur at $w = 2$ and $w = 4$, respectively. These results are consistent with those obtained using the Poincaré map, as presented in Fig. 2. Thus, most of the periodic impact motion can be described as period-n impact-p motion. For example, the period-*1* and period-2 impact-*1* motions appear at $w = 2$ and $w = 4$, respectively.

The bifurcation diagrams in Figs. 2 and 3 reveal a non-periodic (chaotic) region between two impact resonance peaks. For driving frequency ranges that do not correspond to any explicit analytical solution, numerical solutions are provided for the full region of the control parameter. Thus, the boundary of the region for each impact vibration is predicted. Knowledge regarding the position and structure of the stable and unstable regions is essential for implementing practical applications. In the following subsection, the impact vibrations are classified as period-n impact-p motions.

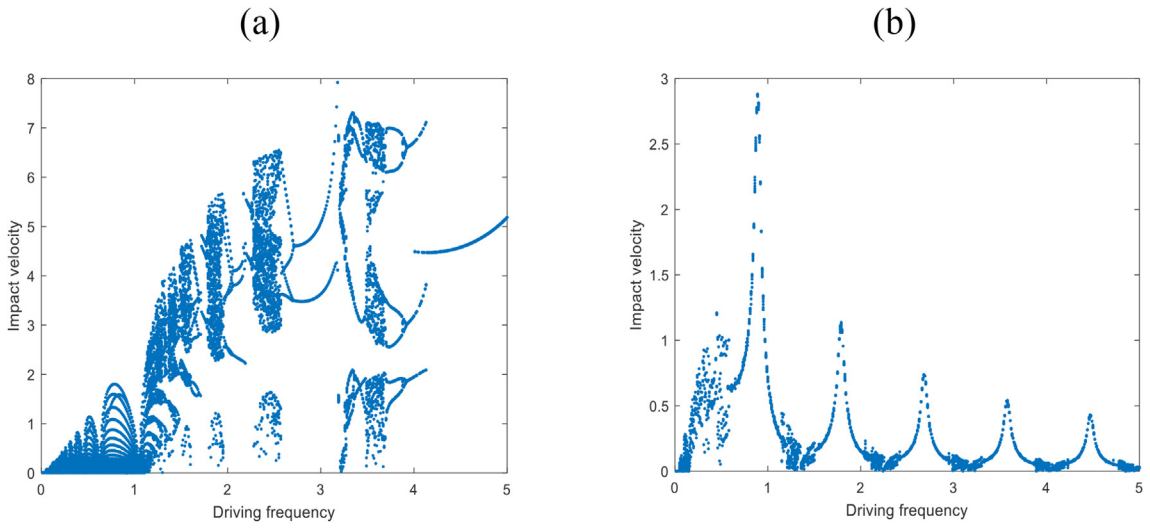

Fig. 12. Effects of mass: (a) m = 0.1; (b) m = 5.

3.1. Sticking motion

Sticking motion is present in regions where $w < 0.25$ and where the oscillator collides with the limited stop at low velocities. This phenomenon produces numerous low impact series, and the vibration eventually becomes stuck at the end-stop. Fig. 4a and b depict the points set on the Poincaré and impact maps when the driving frequency is $w = 0.1$. A motion is represented by a single point on the Poincaré map (period-*1*) and by a sequence of points on the impact map (impact-∞). The impact map indicates that the maximum impact velocity is 0.23 at phase 0.03 and that the sticking occurs at phase 0.11. Fig. 5a and b reveal that when the driving frequency increases to $w = 0.25$, the maximum impact velocity increases to 0.62 at phase 0.08, and the sticking occurs at phase 0.33. These phenomena are referred to as periodic sticking motions and classified as period-*1* impact-∞ motions.

3.2. Chaotic motion I

When the driving frequency increases, the impact vibration does not remain stuck at the limited stop but rather departs after several impacts. The impact motions are complex within the driving frequency region of [0.25, 1] (Figs. 2 and 3); this result further indicates a period-doubling route to chaotic behaviour.

The points set on the Poincaré and impact maps for when the driving frequency $w = 0.75$ are presented in Fig. 6a and b, respectively. The results revealed a complex structure comprising period-*fractal* and impact-*fractal* patterns on the maps. This phenomenon is referred to as a chaotic motion and confirms the instability of the impact motion. When the driving frequency increases to $w = 0.86$, the impact motion converges toward a period-*1* impact-*2* motion. Subsequently, the impact motions remain stable within the region of [0.86, 0.99]. However, when the driving frequency $w = 1.0$, the impact motion starts to bifurcate, again leading to a complex motion (Fig. 7a and b).

3.3. Periodic motion

When the driving frequency $w = 1.4$, the impact motion converges toward a periodic impact motion. When $w = 2$, the maximum impact velocity is reached; the corresponding results are presented with a period-*1* impact-*1* motion in Fig. 8a and b. This phenomenon is referred to as periodic impact resonance.

3.4. Chaotic motion II

The impact motions in the driving frequency region of [2.5, 3.5] are complex (Figs. 2 and 3). The Poincaré and impact maps for when the driving frequency $w = 2.8$ are presented in Fig. 9a and b, respectively. The results indicate a complex structure comprising period-*fractal* and impact-*fractal* patterns on the maps. The period-*fractal*–impact-*fractal* attractor that occurs at $w = 0.75$ is different from that occurring at $w = 2.8$. The impact series at $w = 0.75$ appears to comprise impact velocities of moderate magnitude (range: 0–2.5), whereas the

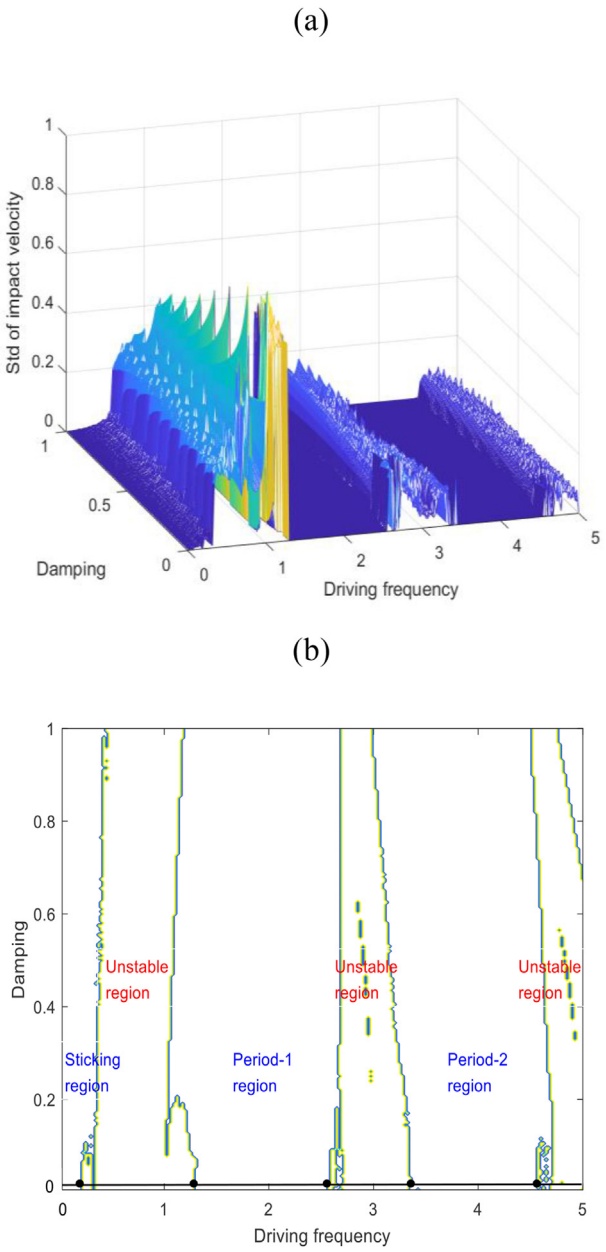

Fig. 13. Stable and unstable boundaries in (w, c) domain.

impact series at $w = 2.8$ comprises impact velocities of low magnitude (range: 0–0.7). Although both of these phenomena are referred to as chaotic motion, they exhibit different patterns on the maps. These results confirm the instability of the impact motions.

3.5. Statistical index of the diagram

To quickly detect impact motions, the *Std* of the impact series in the impact map is calculated as follows:

$$Std = \sqrt{\frac{1}{N}\sum_{i=1}^{N}|I_i - \mu|^2} \tag{2}$$

where μ is the mean of I_i and where I_i is the impact series (velocities) in the impact map. To ensure the accuracy of the results, 5000 impact series are considered, and the first 100 impacts are ignored. Fig. 10 compares the bifurcation diagrams and *Std* values (by a factor of 5) across multiple driving frequencies and reveals that the bifurcation diagram and statistical index (*Std*) results are consistent and in strong agreement. In the low-*Std* regions, the motion is stable, such as the sticking motion in [0, 0.25], the period-*1* impact-*1* motion in [1.5, 2.5], and the period-*2* impact-*1* motion in [3.5, 4.5]. In the large-*Std* and moderate-*Std* regions, the motions are unstable, such as the chaotic motion *I* in [0.25, 1.45] and the chaotic motion *II* in [2.5, 3.5].

4. Control of two parameters

The bifurcation diagram presented in Section 3 is considered by only one control parameter, and the impact series in the maps with the varying driving frequency w are plotted. The details of specific local parameters are investigated through Poincaré and impact mapping. The stable and unstable regions of the driving frequency w are identified. In this section, two control parameters of the bifurcation diagram are considered. The influence of the two-control-parameter domains of (w, m), (w, c), (w, k), (w, f), and (w, r) are investigated for when the fixed clearance $g = 0$. The results are plotted using a mesh of 200 multiplied by 200 points in two-control-parameter domains. For each point, the first 100 impacts are ignored, and the subsequent 5000 impact series are calculated for the statistical index (*Std*).

4.1. Effects of driving frequency and mass

The *Std* values of the impact series in the maps for two control parameters (w, m) for when $g = 0$ are presented in Fig. 11a. The high mountain-like pattern indicates that the *Std* of the impact series is high, indicating unstable motions. The flat area represents small *Std* values, indicating periodic motions. The contour plot of Fig. 11a is presented in Fig. 11b, where the stable and unstable boundaries of the impact motions are classified. In Fig. 11b, the horizontal line represents the indication of *Std* when the mass parameter $m = 1$. This situation is depicted in Fig. 3, where the resonance of free oscillation is $w_n = 1$. Six regions are classified by impact motion at the driving frequency $w = [1, 5]$. The sticking motion is within [0, 0.25]; the period-*1* impact-*1* motion is within [1.25, 2.5]; the period-2 impact-*1* motion is within [3.5, 4.5]; and the unstable motions are within [0.25, 1.25], [2.5, 3.5], and [4.5, 5].

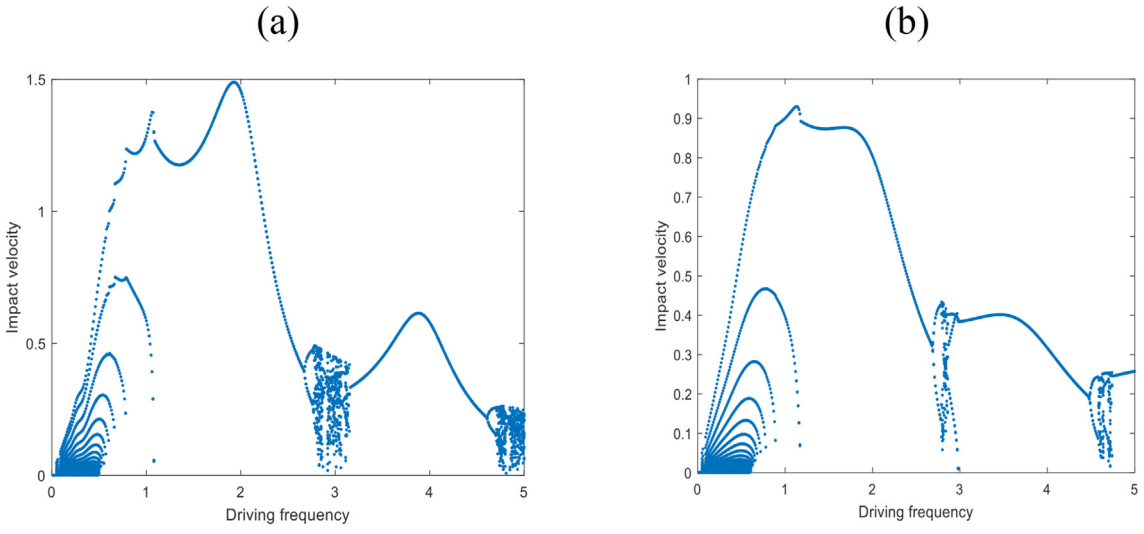

Fig. 14. Effects of damping: (a) c = 0.5; (b) c = 1.

When the mass is small ($m < 1$), the resonance of free oscillation increases. In addition, the impact motions correspond to high *Std* values and increases in the amplitudes of sticking and chattering motions. For example, the bifurcation diagram presented in Fig. 12a represents the situation when $m = 0.1$. The resonance of free oscillation is $w_n = 3.1$, and the first impact resonance is approximately 6.2. Thus, the amplitude on the y-axis is increased to 8. When the mass increases ($m > 1$), the resonance of free oscillation decreases. Consequently, the period-n impact resonances also decrease. For example, the bifurcation diagram presented in Fig. 12b represents the situation when $m = 5$. The resonance of free oscillation is $w_n = 0.44$, and the first impact resonance is approximately 0.88. The period-n impact resonances for $n = 1$ to 5 are presented.

The two-control-parameter bifurcation diagram with a statistical index provides an understanding of various motions that are simultaneously present in the (w, m) domain. This diagram is a useful tool for designing an impact system where stable and unstable boundaries can be used for identification within a two-parameter space.

4.2. Effects of driving frequency and damping

The *Std* values of the impact series in the maps for the two control parameters (w, c) for when $g = 0$ are presented in Fig. 13a. The flat area indicates stable motions, whereas the mountain-like area indicates unstable motions. The contour plot of Fig. 13a is presented in Fig. 13b, where the stable and unstable regions of the impact motions are classified in the (w, c) domain. In Fig. 13b, the horizontal line represents the indication of *Std* when the damping parameter $c = 0.01$; this situation is depicted in Fig. 3. When the damping c increases, the impacting rate and the amplitude of impact resonance are reduced. The situations where $c = 0.5$ and 1 are plotted in Fig. 14a and b, respectively. Thus, when the parameter pair of w and c varies, the stable and unstable boundaries appear in the (w, c) domain.

4.3. Effects of driving frequency and stiffness

The *Std* values of the impact series in the maps for the two control parameters (w, k) for when $g = 0$ are presented in Fig. 15a; in this figure, the flat area indicates stable motions, whereas the mountain-like area indicates unstable motions. The contour plot of Fig. 15a is presented in Fig. 15b, where the stable and unstable boundaries of the impact motions are classified in the (w, k) domain. In Fig. 15b, the horizontal line represents the indication of *Std* when the stiffness parameter $k = 1$. This situation is depicted in Fig. 3, where the resonance of free oscillation is $w_n = 1$. Six regions are classified by impact motion at the driving frequency $w = [1, 5]$.

When the stiffness k decreases, so does the resonance of the free oscillation. Thus, the location of the impact resonances shifts forward, and the

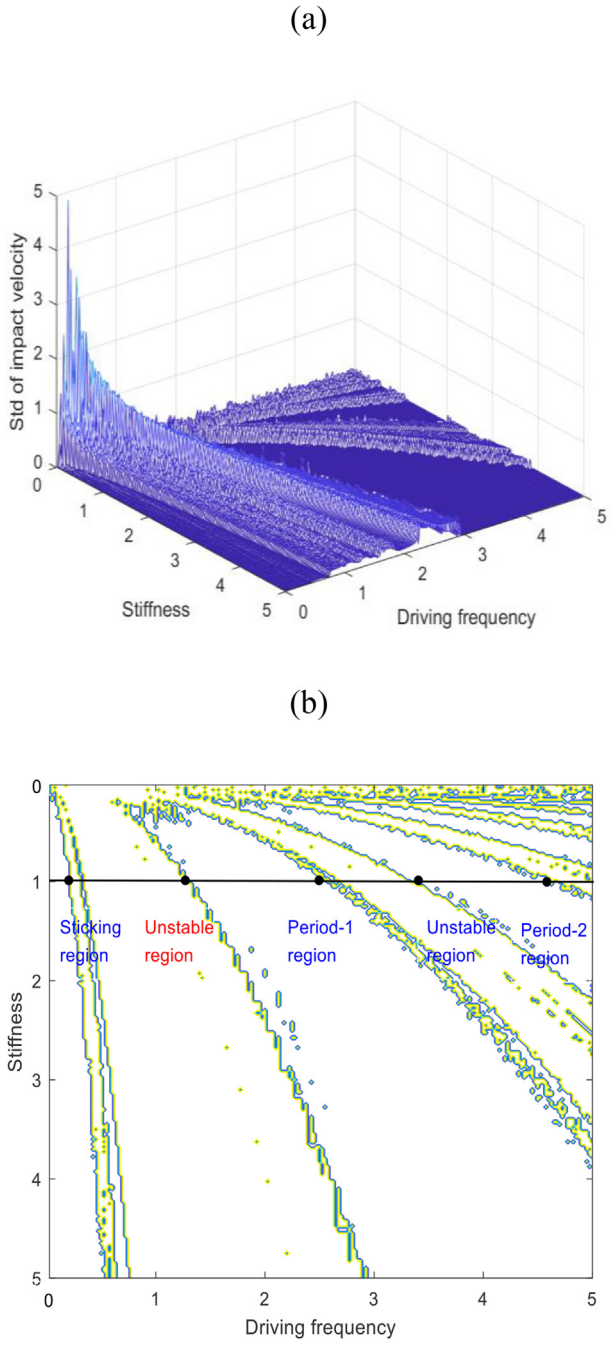

Fig. 15. Stable and unstable boundaries in (w, k) domain.

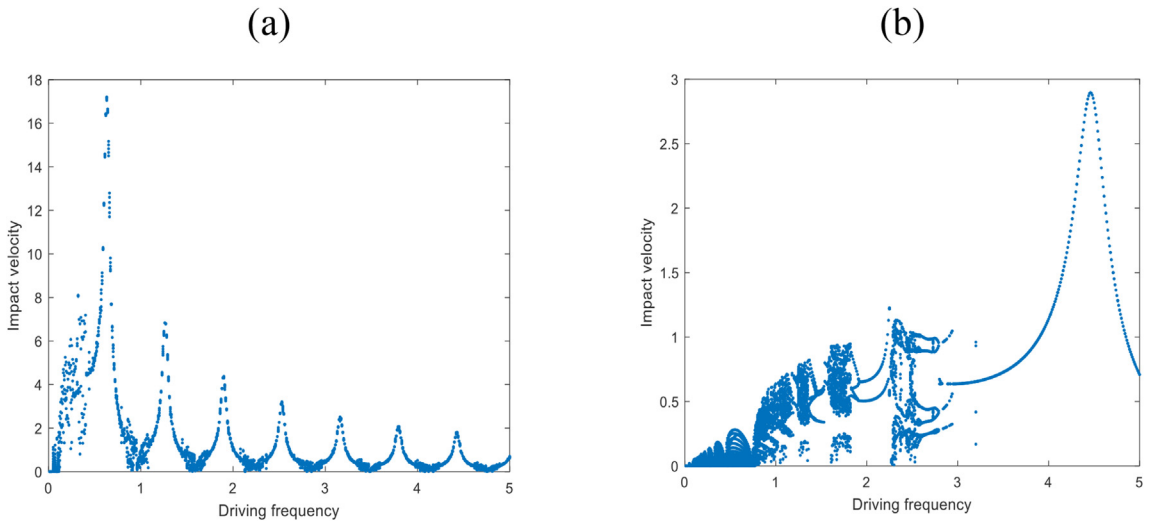

Fig. 16. Effects of stiffness: (a) $k = 0.1$; (b) $k = 5$.

amplitude of the impact motions increases. For example, Fig. 16a presents the bifurcation diagram when $k = 0.1$. The resonance of free oscillation is $w_n = 0.31$, and the first impact resonance is approximately 0.62. Seven impact resonances appear, and the impact magnitude is amplified by a factor of 3 relatives to the situation when $k = 1$. When the stiffness k increases, so do the resonance of free oscillation and the impact motions. As a result, the effect of the impact resonances decreases, and the sticking and chattering motions increase. Fig. 16b presents the bifurcation diagram for when $k = 5$. The resonance of free oscillation is $w_n = 2.23$, and the first impact resonance is approximately 4.46. Thus, the amplitude in the y-axis is reduced to 3.

4.4. Effects of driving frequency and forcing amplitude

The *Std* values of the impact series in the maps for the two control parameters (w, f) for when $g = 0$ are presented in Fig. 17a. The flat area indicates stable motions, whereas the mountain-like area indicates unstable motions. The contour plot of Fig. 17a is presented in Fig. 17b, where the stable and unstable boundaries of the impact motions are classified in the (w, f) domain. In addition, in Fig. 17b, the horizontal line represents the indication of *Std* when the forcing amplitude parameter $f = 1$; this situation is depicted in Fig. 3. When the forcing amplitude f changes, the boundaries of the impact motions in the (w, f) domain remain largely unchanged. The various types of impact motions exhibit similar patterns ($f = 0.1$, Fig. 18a; $f = 5$, Fig. 18b), and the magnitudes of the impact velocities are proportioned to the forcing amplitude.

4.5. Effects of driving frequency and restitution coefficient

The *Std* values of the impact series in the maps for the two control parameters (w, r) for when $g = 0$ are presented in Fig. 19a. The flat area indicates stable motions, whereas the mountain-like area indicates unstable motions. The contour plot of Fig. 19a is presented in Fig. 19b, where the stable and unstable boundaries of the impact motions are classified in the (w, r) domain. In Fig. 19b, the horizontal line represents the indication of *Std* when the restitution coefficient parameter $r = 0.8$; this situation is presented in Fig. 3. When the control parameter of the restitution coefficient r increases, the motions with a high impacting rate occur within the full driving frequency range. Fig. 20a depicts the situation when the restitution coefficient $r = 1$, indicating that two impact resonances dominate the system. The amplitude on the y-axis is increased to 35. In addition, the periodic motions are disrupted by high strength impact responses. Conversely, when the restitution coefficient r decreases, the impact response is attenuated gradually. Fig. 20b depicts the situation when the restitution coefficient $r = 0.1$, at which point the impact resonances are reduced. When the first impact resonance shifts to $w = 1$, the chattering motions decay to sticking motions, and the chaotic motions decay to periodic motions.

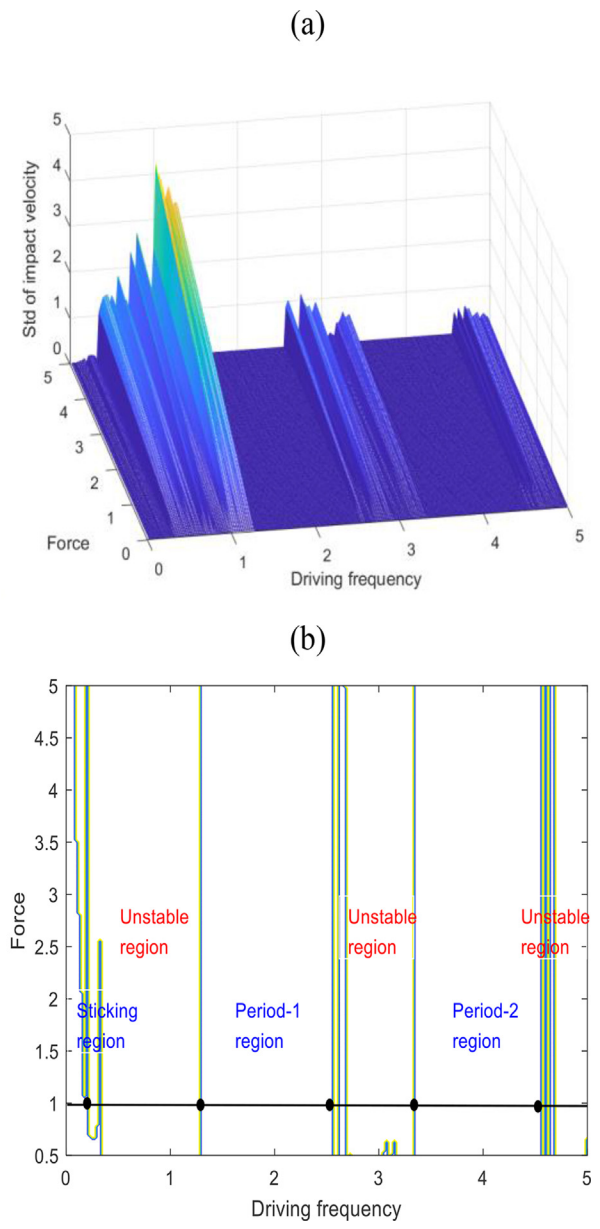

Fig. 17. Stable and unstable boundaries in (w, f) domain.

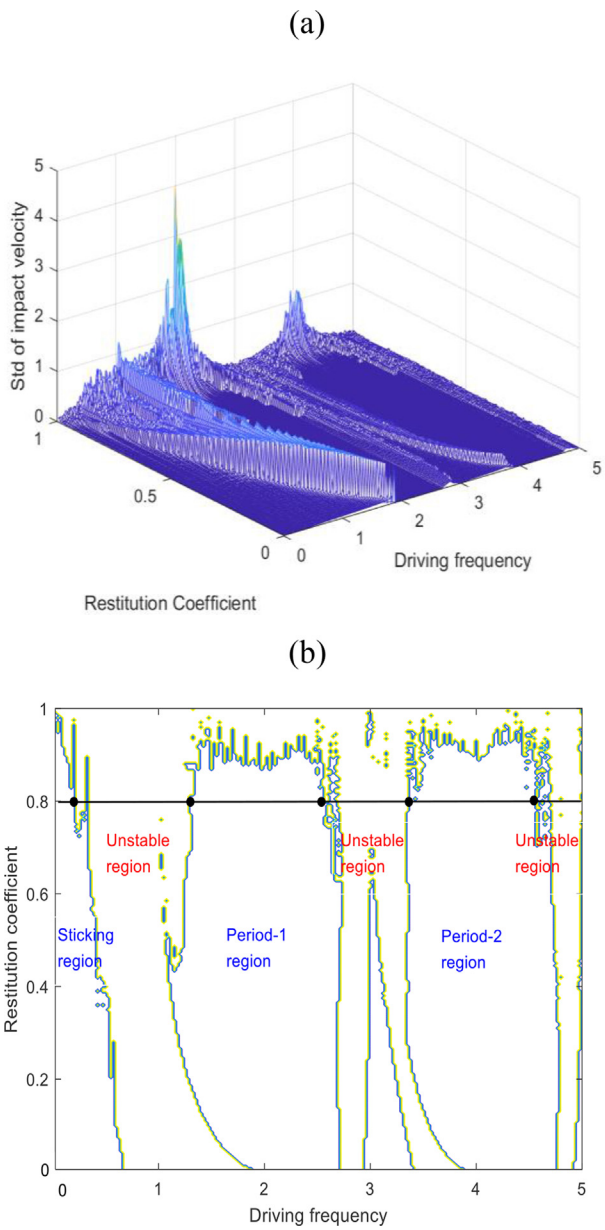

Fig. 19. Stable and unstable boundaries in (w, r) domain.

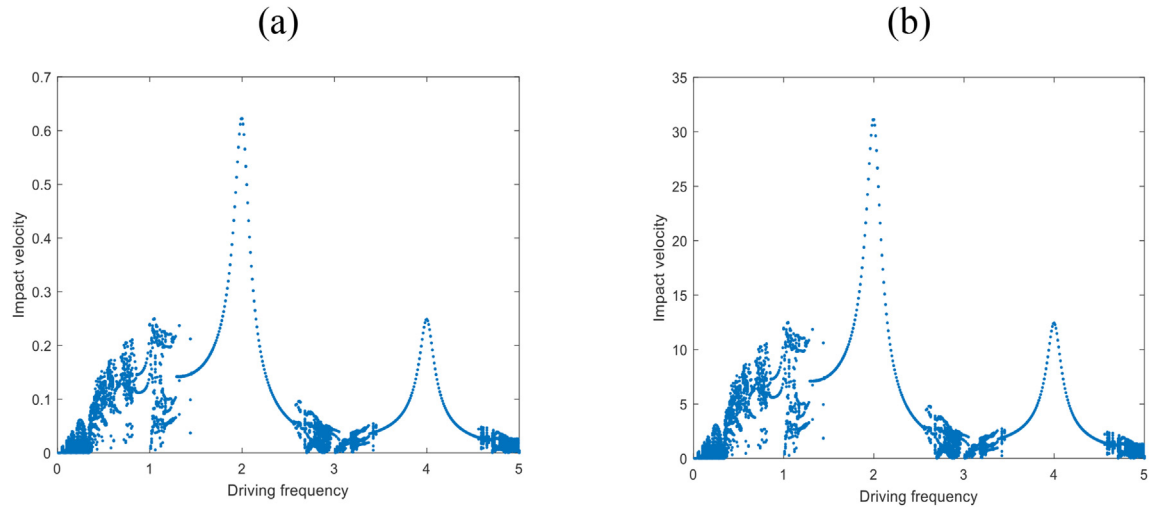

Fig. 18. Effects of forcing amplitude: (a) f = 0.1; (b) f = 5.

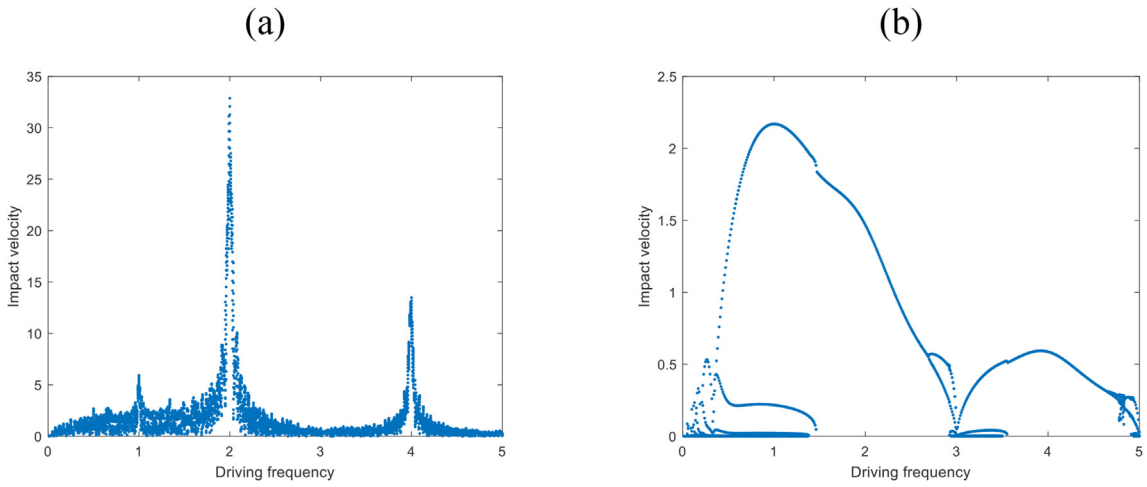

Fig. 20. Effects of restitution coefficient: (a) $r = 1$; (b) $r = 0.1$.

5. Conclusions

In the present study, the sticking, periodic, and chaotic motions are characterised by employing the nonlinear techniques of Poincaré mapping, impact mapping, and bifurcation diagram plotting. To minimize the computing cost, the statistical index of *Std* is calculated using impact series in maps. The results for the bifurcation diagram and statistical index *Std* are consistent and in strong agreement within the driving frequency region. Therefore, the *Std* values for the two control parameters of (w, m), (w, c), (w, k), (w, f), and (w, r) are calculated. In the generated three-dimensional plots, the mountain-like area indicates unstable regions, whereas the flat area indicates stable regions. Finally, the corresponding contour plots display the boundaries of the stable and unstable motions in the two-control-parameter domain. The present findings expand our understanding of impact vibration and how it benefits condition monitoring.

Declaration of conflicting interests

None.

References

[1] Goyder H, The C. A study of the impact dynamics of loosely supported heat exchanger tubes. J Pres Vessel Technol 1989; 111:394–401.
[2] Jiang J, Zhang B. Rolling element bearing vibration modelling with applications to health monitoring. J Vib Control 2011;18:1768–76.
[3] Kadmiri Y, Rigaud E, Perret-Liaudet J, Vary L. Experimental and numerical analysis of automotive gearbox rattle noise. J Sound Vib 2012;331:3144–57.
[4] Moosavian A, Najafi G, Ghobadian B, Mirsalim M, Jafari SM, Sharghi P. Piston scuffing fault and its identification in an IC engine by vibration analysis. Appl Acoust 2016;102:40–8.
[5] Cheng H, Zhang Y, Lu W, Yang Z. Mechanical characteristics and nonlinear dynamic response analysis of rotor-bearing-coupling system. Appl Math Model 2021;93:708–27.
[6] Thompson JMT. Complex dynamics of compliant offshore structures. Proc Roy Soc Lond 1983;387:407–27.
[7] Grace IM, Ibrahim RA, Pilipchuk VN. Inelastic impact dynamics of ships with one-sided barriers. Part I: analytical and numerical investigations. Nonlinear Dynam 2011;66: 589–607.
[8] Grace IM, Ibrahim RA, Pilipchuk VN. Inelastic impact dynamics of ships with one-sided barriers. Part II: experimental validation. Nonlinear Dynam 2011;66:609–23.
[9] Chen M, Taylor RE, Choo YS. Investigation of the complex dynamics of float-over deck installation based on a coupled heave-roll-pitch impact model. Ocean Eng 2017;137: 262–75.
[10] Chen M, Xiao P, Zhang Z, Sun L, Li F. Effects of the end-stop mechanism on the nonlinear dynamics and power generation of a point absorber in regular waves. Ocean Eng 2021; 242:110123.
[11] Guo B, Ringwood JV. Non-linear modelling of a vibro-impact wave energy converter. IEEE Trans Sustain Energy 2021;12:492–500.
[12] Hunt KH, Crossley FRE. Coefficient of restitution interpreted as damping in vibroimpact. J Appl Mech 1975;42:440–50.
[13] Silva MR, Marques F, Silva MT. A compendium of contact force models inspired by Hunt and Crossley's cornerstone work. Mech Mach Theor 2022;167:104501.
[14] Shaw SW, Holmes PJ. Periodically forced piecewise linear oscillator. J Sound Vib 1983;90:129–55.
[15] Nordmark AB. Non-periodic motion caused by grazing incidence in an impact oscillator. J Sound Vib 1991;145: 279–97.
[16] Nordmark AB, Kowalczyk P. A codimension-two scenario of sliding solutions in grazing-sliding bifurcations. Nonlinearity 2006;19:1–26.
[17] Foale S, Bishop SR. Dynamical complexities of forced impacting systems. Phil Trans Roy Soc Lond 1992;338: 547–56.
[18] Chillingworth D. Dynamics of an impact oscillator near a degenerate graze. Nonlinearity 2010;23:2723–48.
[19] Budd C, Dux F. Intermittency in impact oscillators close to resonance. Nonlinearity 1994;7:1191–224.
[20] Budd C, Dux F. The effect of frequency and clearance variations on single-degree-of-freedom impact oscillators. J Sound Vib 1995;184:475–502.
[21] Lee JY. Motion behaviour of impact oscillator. J Mar Sci Technol 2005;13:89–96.

[22] Samukham S, Khaderi SN, Vyasarayani CP. Galerkin-Lvanov transformation for nonsmooth modeling of vibro-impacts in continuous structures. J Vib Control 2021;27:1548−60.
[23] Skurativskyi S, Kudra G, Wasilewski G, Awrejcewicz J. Properties of impact events in the model of forced impacting oscillator: Experimental and numerical investigations. Int J Non Lin Mech 2019;113:55−61.
[24] Witkowski K, Kudra G, Wasilewski G, Awrejcewicz J. Mathematical modelling, numerical and experimental analysis of one-degree-of-freedom oscillator with Duffing-type stiffness. Int J Non Lin Mech 2022;138:103859.
[25] Lee JY, Yan JJ. Control of impact oscillator. Chaos, Solit Fractals 2006;28:136−42.
[26] Chang SH, Hu JF, Lue YF. Nonlinear dynamics and controlling chaos in a magnetic levitation system. J Mar Sci Technol 2018;26:604−10.
[27] Wei X, Li N, Ding W. Chaotic motion control of a vibro-impact system based on data-driven control method. J Vib Control 2023;29:148−57.